Laser-driven pointed acceleration of electrons with preformed plasma lens

K. A. Ivanov,[1,2,*] D. A. Gorlova,[1,3] I. N. Tsymbalov,[1,3] I. P. Tsygvintsev,[4] S. A. Shulyapov,[1] R. V. Volkov,[1] and A. B. Savel'ev[1,2]

[1]*Faculty of Physics, Lomonosov Moscow State University, 119991 Moscow, Russia*
[2]*Lebedev Physical Institute of Russian Academy of Sciences, 119991 Moscow, Russia*
[3]*Institute for Nuclear Research of Russian Academy of Sciences, 117312 Moscow, Russia*
[4]*Keldysh Institute of Applied Mathematics of Russian Academy of Sciences, 125047 Moscow, Russia*

(Received 21 October 2023; accepted 1 May 2024; published 17 May 2024)

The simultaneous laser-driven acceleration and angular manipulation of the fast electron beam are experimentally demonstrated. The bunch of multi-MeV energy charged particles is generated during the propagation of the femtosecond laser pulse through the near-critical plasma slab accompanied by plasma channeling. Plasma is formed by the controlled breakdown of a thin-tape target by a powerful nanosecond prepulse. The electron beam pointing approach is based on the refraction of a laser pulse in the presence of a strong radial density gradient in the breakdown of the tape with a small displacement of the femtosecond laser beam relative to the breakdown symmetry axis. A shift of several micrometers makes it possible to achieve beam deflection by an angle up to 10° with acceptable beam charge and spectrum conservation. This opens up opportunities for *in situ* applications for scanning objects with an electron beam and the multistage electron beam energy gain in consecutive laser accelerators without bulk magnetic optics for particles. Experimental findings are supported by numerical particle-in-cell calculations of laser-plasma acceleration and hydrodynamic simulations.

DOI: 10.1103/PhysRevAccelBeams.27.051301

I. INTRODUCTION

The generation of energetic collimated electron beams with a high charge using laser-plasma accelerators has become one of the main area of application for terawatt (TW) and petawatt (PW) laser systems [1–3]. Thanks to laser wakefield acceleration (LWFA) [4,5] and direct laser acceleration (DLA) [6,7] in the relativistic plasma channel, together with the rapid development of high repetition rate TW-class lasers, the new phenomena related to astrophysics [8], nuclear photonics [9], biomedicine, and diagnostics [10,11], etc. have become available to a wide community of researchers literally within the laboratory. The latter circumstance imposes fairly severe restrictions on the size of laboratory sources utilizing compact laser systems with peak power of up to 100 TW (including new-generation systems with peak power of a few TW with a repetition rate up to a kHz level [12]). Besides, the design of the electron beam generator itself (target assembly and adjacent elements) must have reasonable dimensions and provide simple and stable operation as well as control over the beam. One should also consider the bunch acceleration efficiency in terms of mean energy and charge. Instead of a single accelerating stage by an extremely powerful laser pulse the use of a few laser pulses can provide consecutive bunch energy gain in a number of acceleration stages driven by less-demanding and modest laser systems [13–15].

For various application scenarios, the angular targeting and pointing of the electron beam are of key importance, whether it concerns the optimal injection into the subsequent stage of acceleration [16–18], injection schemes [19] relevant to the AWAKE experiment [20], scanning of a sample, directing the bunch into different detectors, radio medicine applications, including FLASH therapy [21], etc. For this, standard accelerator technology can be used: magnetic lenses and dipoles. But their key drawback is high energy selectivity, whereas the laser acceleration of particles beam with high charge leads to rather wide energy spectrum [22]. Also worth noting the bulkiness and slow adjustment of magnetic optics. Therefore, the issue of controlling the beam pointing is of great importance not only from the point of view of compactness but also the preservation of a high charge. For these purposes, several purely plasma methods have been proposed for the LWFA scheme. Among them, we can single out the waveguide propagation of a pulse, when a laser beam is introduced onto the axis of an electron bunch through a curved plasma channel [23,24]. It was also proposed to use a pulse with an inclined wave front, which

*akvonavi@gmail.com

will turn in a low-density plasma and take the electron beam behind it in the wakefield acceleration mode [25,26].

In this work, we experimentally demonstrate the possibility of controlling the ejection angle of an electron bunch with particle energy exceeding a few MeV accelerated by a 1 TW laser pulse in a plasma channel. The latter is formed in a plasma sheet of near critical density when a thin (15 μm) mylar tape is hole bored by an additional nanosecond prepulse (100 mJ, 8 ns, 10^{13} W cm^{-2}), coming ahead of the main accelerating femtosecond pulse (50 mJ, 50 fs, 5×10^{18} W cm^{-2}) by a few nanoseconds. The prepulse forms a breakdown with strong radial density gradient. Precise adjustment of the breakdown axis with respect to the femtosecond pulse axis makes it possible to control the trajectory of the relativistic plasma channel due to laser beam refraction. The accelerated electron beam preserves its characteristics (energy, spectrum, and divergence) at a high degree. The findings are confirmed by simulations and analytical model.

II. MAIN EXPERIMENTAL RESULTS

Previously, we proposed a laser-driven electron beam source using subcritical plasma and moderate peak power (1 TW) laser system delivering bunches of particles with a high charge at 10 Hz repetition rate [27]. For this plasma with an optimal electron density, longitudinal profile was formed by an intense nanosecond prepulse focused onto the surface of a thin plastic tape target. Propagation of the femtosecond pulse few nanoseconds after the peak of the prepulse through the plasma led to self-focusing, channelling in plasma, and direct laser acceleration of particles. In the current experimental campaign, we followed this approach with modified setup (Fig. 1).

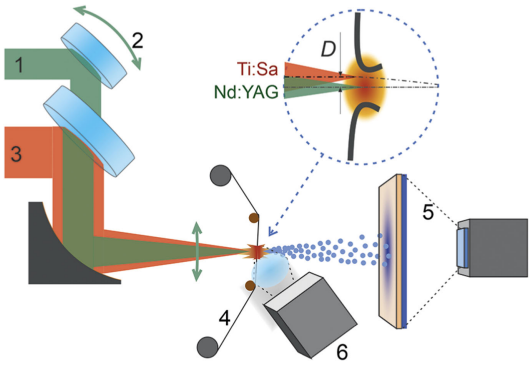

FIG. 1. Experimental scheme: 1—Nd:YAG nanosecond prepulse, 2—adjustable mirror for Nd:YAG radiation, 3—femtosecond pulse, 4—tape target, 5—electron beam detector (Lanex scintillation screen and camera with lens), 6—camera with microobjective collecting the scattered light from plasma (perpendicular to observer), *D*—deviation of the Ti:Sa laser pulse axis relative to the Nd:YAG axis (target breakdown symmetry axis).

The femtosecond pulse with energy 50 mJ was focused into a 4.0 ± 0.2 μm FWHM spot ($F/D = 6.5$) to an estimated vacuum peak intensity $\approx 5 \times 10^{18}$ W cm^{-2} onto the surface of 15 μm thick transparent mylar (PET) tape target. During the tape rewind, the target surface position was stable within the Rayleigh length. The laser was almost normally incident on the target. A small angle of roughly 10° was introduced in order to avoid back reflection of laser radiation into the optical compressor. The relative amplitude of the amplified spontaneous emission pedestal in the domain 10–100 ps prior to the main pulse was 10^{-8} measured by third order autocorrelator.

The prepulse intensity was 10^{13} W cm^{-2} with a focal spot diameter 13 μm (FWHM). The optimal delay for the electron beam generation was ~2 ns. The optimal delay between the peaks of the pulses depends on the target thickness and prepulse intensity, since it determines nanosecond plasma evolution dynamics of the tape target. The density and hence refractive index distribution created by the nanosecond pulse is radially dependent and the plasma acts as a lens: one can estimate the laser beam refraction under its propagation with a small deviation *D* from the longitudinal symmetry axis of the plasma hole in the tape target. For this, we implemented the updated experimental setup that makes possible to shift the axis of the heating nanosecond pulse with respect to the femtosecond pulse axis by tilting the mirror (2) in the Nd:YAG laser path.

The alignment of the axes of nano- and femtosecond pulses was controlled by transferring images of the waist of the off-axis parabolic mirror by a micro-objective to a CCD camera with a high optical resolution. The discreteness of the *D* was determined by a stepper actuator on the mount of the Nd:YAG laser mirror and was 2.5 ± 0.5 μm. The electron beam was detected on a Lanex scintillating screen in the direction of laser radiation. A metal filter (300 μm of tungsten) directly in front of the scintillator cut off electrons with energies below ~3 MeV without strong additional beam divergence after scattering in the filter. A magnetic spectrometer with field strength 0.5 T could be introduced into the electron beam path instead of Lanex screen detector for energy distribution evaluation. The total charge of the beam was measured by means of photonuclear technique [28]. For this, a tungsten 2 mm thick plate was used to attenuate the electrons and generate Bremsstrahlung, which was absorbed by a beryllium $4 \times 4 \times 3$ cm cube placed after the plate, where (γ,n) reaction with a threshold of 1.6 MeV produced neutrons detected by set of He-3 counters. Scattered light from the plasma in the visible range was also detected in the perpendicular to the laser propagation plane as the femtosecond pulse passed through the tape. For this, the region of interest was imaged to a CCD camera using a microobjective.

Figure 2 (left column) illustrates averaged over 100 shots images of the electron beam on the Lanex screen for coaxial propagation of femtosecond and nanosecond pulses (a),

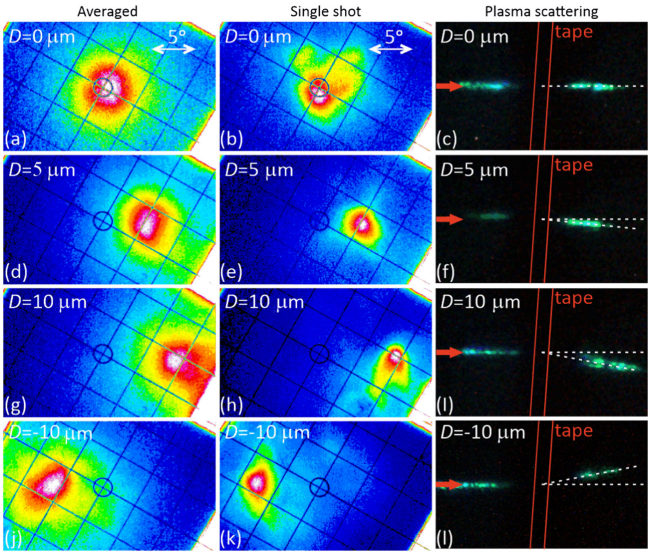

FIG. 2. Electron beam stamps on the Lanex detector averaged (first column) and single shot (second column) as well as plasma scattered light signal (third column) at $D = 0$ μm (first row), 5 μm (second row), 10 μm (third row), and −10 μm (forth row). Red arrow indicates the incident laser beam direction. The red lines mark the tape initial position.

and for $D = 5$ (d), 10 (g), and −10 μm (j). The observed electron beam displacement at $D = 10$ μm on the Lanex detector corresponds to an angle of deflection from the original axis by ∼10°. The angular stability of the electron beam is estimated below 0.15 rad. One can also notice the similar beam deflection for positive and negative D. This demonstrates that the breakdown symmetry is not significantly affected by the laser radiation angle of incidence onto the target. The shot to shot fluctuations of the beam across the detector are due to the instabilities of the transverse intensity distribution across the focal spot of the nanosecond laser, the temporal jitter of the Q-switch, which ultimately affect the breakdown parameters in the tape. In single shots (see examples in the second column in Fig. 2), the beam divergence is estimated as 0.08 ± 0.02 rad. The image of the plasma channel scattered light follows the electron beam as seen in the third column in Fig. 2. It is worth noting that the absolute position of the tape relative to the waist of the femtosecond beam did not require adjustment in the case of a transverse displacement of the breakdown axis. This greatly simplifies the handling of electron beam for applications.

A single shot typical energy spectrum of an electron bunch is presented in Fig. 5 for $D = 0$ μm. The exponential distribution is observed. The total charge Q for electrons with energy above 1.6 MeV was estimated as 30 ± 7 pC by photonuclear technique without observable dependence on deviation. The spectrum of deflected bunch was not assessed due to complexity of the spectrometer alignment. One can rely on the electron beam stamps and luminosity of the Lanex screen, where the average scintillation brightness, overall shape of the stamp and divergence remained constant when varying D. This suggests that the energy gain mechanism is kept the same, and the beam charge did not vary significantly. A comparison of experimentally measured beam parameters with numerical estimations may be found in Figs. 5 and 7.

III. NUMERICAL SIMULATIONS AND DISCUSSION

The deflection angle of the laser beam θ during propagation along the Oz axis is determined by the change in the refractive index n along the radial coordinate: $\frac{d\theta}{dz} = n^{-1}\frac{dn}{dr}$. Whereas, according to the Drude model, the refractive index depends on the electron density n_e in plasma. The preformed plasma with radial density gradient acts as a lens, leading to the refraction of the femtosecond pulse. Additional modulation into the local refractive index (which causes, in particular, the formation of a plasma channel) is introduced by field ionization and the ponderomotive action of light during the relativistic laser pulse propagation through the plasma. We made hydrodynamic simulations of the tape ablation by the nanosecond laser pulse. Then PIC simulations of the electron acceleration process using the simulated plasma profile were performed. PIC simulations were made for different deviations D from the plasma longitudinal axis. The target ablation and boring was modeled in hydrodynamic software package 3DLINE [29]. The one-temperature one-fluid model of a quasineutral plasma was used. The local ionization multiplicity was determined from the stationary distribution obtained in the framework of collisional-radiative equilibrium using the THERMOS code [30]. This approximation works well on the considered scale of characteristic times (∼ns) and laser intensities (10^{12}–10^{13} W cm^{-2}), and detailed consideration of the ionization kinetics is not required. The equation of state was calculated using the Thomas-Fermi model with semiempirical corrections in the phase transition region using the FEOS code [31]. The target material was PET (initial density 1.38 g/cm^3, temperature 270 K), thickness 15 μm. The laser parameters were similar to the experiment: 1064 nm, 8 ns pulse duration FWHM, peak intensity 10^{13} W cm^{-2}. The simulation was carried out in the two-dimensional axially symmetric (r, z) geometry on a fixed grid with a size of 0.5×0.945 mm. Figure 3 illustrates the resulting distribution of ions concentration with strong radial dependence. The data for the optimal delay were then integrated into the PIC code SMILEI [32]. We first carried out 3D modeling to ensure the accurate reproduction of the experimental conditions in the case of co-axial propagation of the two pulses. The target initially consisted of neutral carbon. To save computational time and resources, the simulations with shifted propagation from the symmetry axis were performed in simplified 2D3V geometry. The time step was 0.083 fs, box size

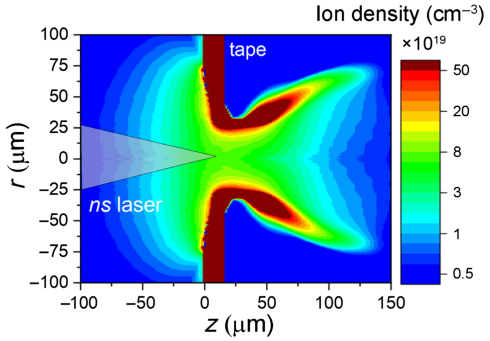

FIG. 3. Calculated distributions (r, z) of the ions concentration in plasma of the PET tape.

$-X = 200\lambda$ (propagation axis), $Y = 80\lambda$ in 2D, and $X = 200\lambda$, $Y = Z = 24\lambda$ in 3D, laser wavelength $\lambda = 0.8$ μm, spatial resolution $-\lambda/32$ in 2D and $\lambda/32$ (along X), and $\lambda/4$ (along Y, Z) in 3D. Several transversal shifts 2.5–20 μm were simulated. The 50 fs pulse was focused in a 4 μm spot FWHM at the front surface of the nonperturbed tape with normalized vector potential $a_0 = 1.5$, where $a_0 \approx 0.85\sqrt{I\lambda^2}$, which corresponds to the experimentally available peak intensity of $\sim 5 \times 10^{18}$ W cm^{-2}.

It is important to underline the main stages of acceleration. The femtosecond laser pulse enters plasma plume and excites plasma waves due to backward Raman scattering. This takes place for the electron density of 0.1–0.2 n_{cr} (see density modulation in Fig. 4(a), where $x/\lambda = 60$ corresponds to the initial surface of the tape target). Wave-vector components near $k_x/k_{x0} = \pm 2$ corresponding to this process appear on the wave-vector diagrams (k_x, k_y),

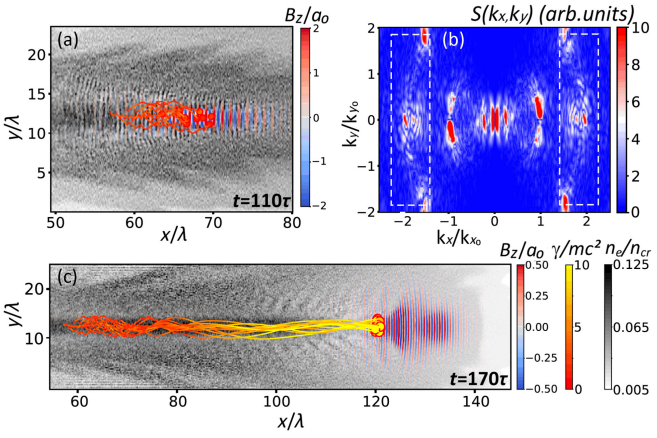

FIG. 4. Magnetic field of the laser pulse in units of a_0 at different 3D PIC simulation periods at the background of electron density in units of n_{cr} (a), (c). Typical trajectories of particles with energy over 3 MeV at the end of simulation are showed by curves, where the color corresponds to particles energy. In (b), the wave-vectors diagram for (a) is demonstrated, where k_0 is the laser wave vector. Color bars for electron energy and density are identical in (a) and (c).

see Fig. 4(b), where k_0 is the laser central wave vector. At the same time, the laser beam is self-focused enhancing the peak intensity [in Fig. 4(a) field amplitude reaches $a_0 = 2.2$] and forming the plasma channel. Breaking of the plasma waves together with ionization of inner atomic shells results in particles injection into the channel. Trajectories of the particles forming the final beam originate near $x/\lambda = 60$–70 [Fig. 4(a)]. Plasma channel with a high field amplitude persists at a distance of a few tenths of micrometers (up to $x/\lambda = 100$) [see Fig. 4(c)]. The transverse oscillations of electrons are transformed into longitudinal momentum as seen from trajectories, marked in Fig. 4(c), in accordance with the DLA concept [33]. The particles gain energy in the channel within a few betatron oscillations [the color of the trajectories in Fig. 4(c), i.e., the energy is quickly saturated] and then go out of synchronism, still being trapped by the channel walls though. In the rarefied plasma at the back side of the target, the pulse self-modulates, see Fig. 4(c), and excites longitudinal plasma waves, which do not affect the acceleration process. The analysis of electron energy gain mechanism may be also found in our previous work [27], here we would like to focus onto deflection of the femtosecond and electron beams while passing through the plasma slab with radial dependence of the electron density. It should be noted that this effect can be used not only to deflect a laser beam (as well as an electron beam [25]) but also to diagnose the transverse plasma inhomogeneity itself [34,35]. The principle difference between the 2D and 3D simulations occurs in the modeling of self-focusing [36] resulting in a longer lasting channel in the 3D case. Figure 5(a) demonstrates the compared evolution of the magnetic field B_z in units of a_0 of the pulse in 3D/2D. The B-field amplitude is intentionally saturated for a better observation. The trailing part of the laser pulse diverges stronger in the 2D model during the propagation in the channel. This affects the accelerated electron beam divergence: ~0.5 rad in the 2D and ~0.1 rad in the 3D, evaluated as the FWHM of the angular distribution of the number of particles $\frac{dN}{d\theta}$, see Fig. 5(b). Nevertheless, the typical for the DLA quasiexponential spectra $\frac{dN}{dE}$ in these two cases, Fig. 5(c), reasonably match in terms of shape (above 1 MeV) and maximal energy. The estimation of beam spectrum and divergence in 3D correlates well with experimental measurements of electron beam.

Figures 6(a) and 6(c) represent a wider image of the beam propagation, ionization, and particles motion in the simulation box (2D) with the axial and shifted ($D = 10$ μm) geometry. The concentration gradient promotes the beam deflection. As a result, the plasma channel also deviates from the original axis with conservation of its properties. It is important to note that the laser beam deflects mainly in the region of higher plasma density near the initial tape position, where the electron concentration n_e after ionization lies in the range 0.1–0.2 units of critical

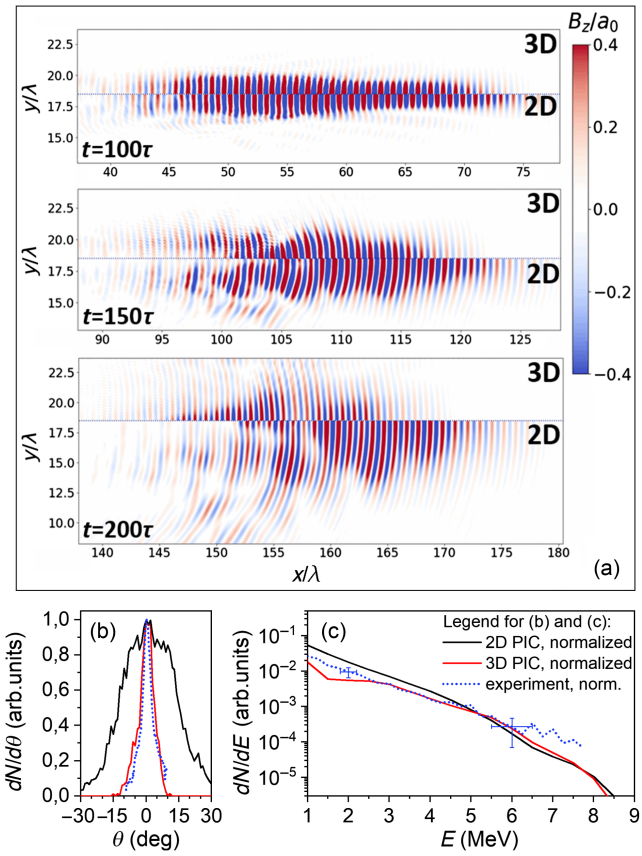

FIG. 5. Comparison of magnetic field of the laser pulse in 3D and 2D at different simulations periods (a). Normalized angular distribution of particles with energy E over 3 MeV (b) and energy spectra (c). In (b), the dashed experimental curve corresponds to Fig. 2(k).

density n_{cr} (for 800 nm radiation $n_{cr} = 1.7 \times 10^{21}$ cm^{-3}). This is supported by the ray-tracing through graded-index medium by solving the eikonal equation proposed by Sharma *et al.* [37]: $\frac{d}{ds}[n(\vec{r})\frac{d\vec{r}}{ds}] = \nabla n(\vec{r})$, where $\vec{r}$ is the position vector of the ray relative to origin, ds is the element of the beam path, and $n(\vec{r})$ represents the refractive index distribution. The solution by fourth order Runge-Kutta method is shown by the dashed lines in Figs. 6(a) and (c). It does not consider self-focusing but clearly depicts the refraction in the preformed plasma lens. The resulting effect in the bent channel is the simultaneous deflection of the accelerated electron bunch since they are guided by the channel fields. Figures 6(b) and 6(d) represent the angular energy spectra of the electron beam. As mentioned above, the overall divergence is high due to peculiarities of 2D modeling. Nevertheless, the angular spectrum of the beam is conserved when accelerating it in curved plasma channel.

The applicability of the proposed method of electron beam deflection for laser systems with other than considered parameters lies in the field of criteria that should be met for efficient particles acceleration in DLA scheme:

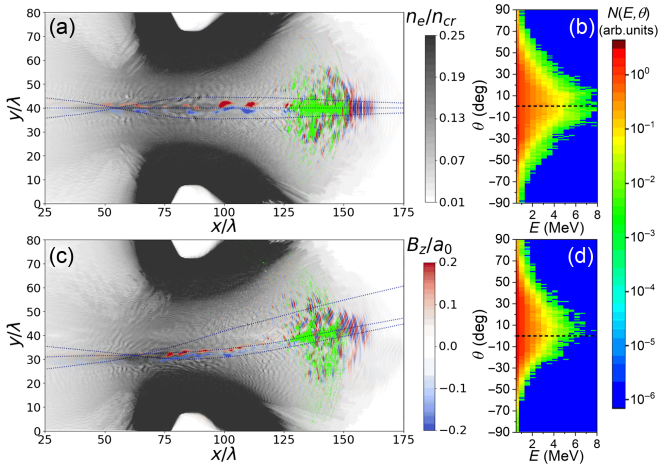

FIG. 6. Results of numerical 2D PIC calculations: normalized magnetic field in the box at the background of normalized electron density during propagation of a femtosecond pulse (left) and angular-energy spectra of accelerated electrons (right) with deviation $D = 0$ (a), (b) and 10 μm (c), (d). Green dots mark electrons with energies above 3 MeV. The blue dashed lines represent the results of ray tracing of a laser beam through an inhomogeneous plasma. Indicated color scales for electron density, magnetic field amplitude, and angular spectra are the same for $D = 0$ and 10 μm.

channeling in plasma, trapping of particles and guidance in the channel [6,7,33]. From this point of view, the focusing of the laser pulse is an important parameter. It is worth noting that despite the maximal energy and charge being related to a_0, tight focusing may not be optimal [38]. In case of modest ~TW lasers in general efficient laser-plasma coupling and DLA requires a more precise parameters adjustment compared to powerful lasers. Focusing with a small F/D number will result in shorter length of channel and stage of DLA, whereas at loose focusing laser pulse may experience ionization defocusing [39] hampering channel formation. Plasma profile also plays an important role. The curvature of the channel is limited by the necessity to retain the particles within the plasma channel—a particle with sufficiently high magnitude of the momentum projection along the channel radial density gradient can overcome the holding quasistatic fields and leave the channel.

The basic beam quality parameters are summarized in Fig. 7 in dependence on the deviation D of the driver pulse for two values of a_0. The laser pulse begins to pass over the denser plasma region at $D > 10$ μm, where due to the modest peak intensity ($a_0 = 1.5$), the acceleration regime related to channeling and DLA struggles to evolve efficiently, which is seen as decrease of electrons energy, Fig. 7(a). Our simulations with increased peak intensity [$a_0 = 2.2$, Fig. 7(b)] demonstrate that this effect is less pronounced, supporting our estimates on experimental applicability of the method at a higher intensity level and increased particles energy. One can also notice that

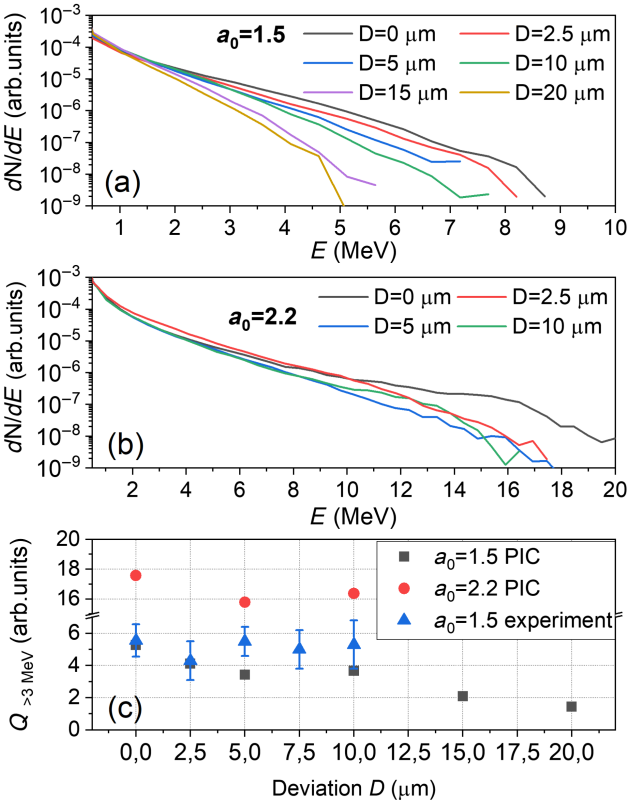

FIG. 7. Energy spectra of the electron beam at varied driver laser beam deviation D from symmetry axis for the vector potential $a_0 = 1.5$ (a) and $a_0 = 2.2$ (b). The relative charge Q of the electron beam for particles above 3 MeV in dependence on the D (c).

charge of the bunch is almost the same independently of the deviation D with $a_0 = 2.2$, Fig. 7(c). As mentioned above, the divergence in the 2D simulations is higher as compared to the 3D and the experiment. However, the angular spread does not tend to widen in the investigated range of D being in agreement with the experimental data. We also put on this graph the total amplitude of the Lanex signal contained in the FWHM around the center of mass of the beam stamp on the detector roughly representing the total number of particles [40], i.e., the relative charge of the beam. Since these measurements provide only relative values, the data point corresponding to experimental charge at $D = 0$ is intentionally put near the first PIC point.

A similar effect, considered earlier in the context of wakefield acceleration, led to a transverse inhomogeneity of the plasma wave, the accelerating longitudinal and focusing transverse fields of which deflected the accelerated electron beam following the laser driver [23,25]. The deviation of the components of the laser field from the initial direction itself determines the change in the trajectory of the accelerated electron. The effect of electron beam small angular deflection in the wake was also discussed in terms of transverse density gradient in gas jet outflow [41]. Recently, the acceleration of electrons in the curved plasma

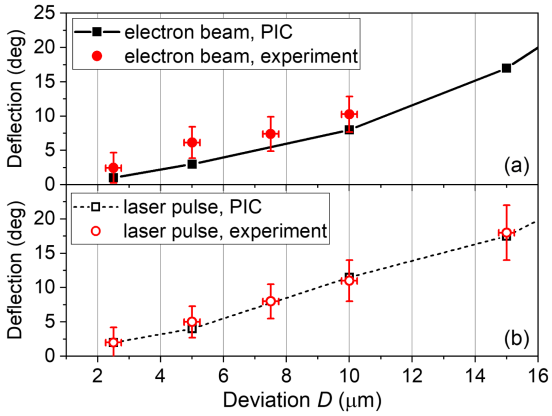

FIG. 8. Numerical and experimental data on the deflection of the electron beam (a) and the laser pulse (b) as a function of the femtosecond pulse deviation D relative to the breakdown symmetry axis.

channel was demonstrated experimentally [42]. Within the framework of the plasma model of an ablated and bored thin tape, one can conclude that key bunch parameters (charge, spectrum, and divergence) are retained acceptable and comparable to the coaxial propagation in a wide range of deviations from the central axis ensuring beam deflection up to 10°. When further increasing D, the laser pulse hits denser layers, and the acceleration regime becomes affected. Nevertheless, already small displacements evidently change the electron beam propagation axis by several degrees, which is more than enough for the beam deflection from its initial axis in whole range of particles energies without the use of energy selective magnetic optics.

The summary of our studies with experimental data on the pulse and electron beam deflection (evaluated from scattered light signal and Lanex screen correspondingly) and comparison with numerical results are presented in Fig. 8, where a good correlation is observed. This indicates that the numerical model of the tape target boring by the nanosecond prepulse is consistent with the experiment. Moreover, one can rely on the good evaluation of the electron bunch acceleration mechanism established numerically.

IV. CONCLUSIONS

The angular manipulation of a laser-generated electron beam during its acceleration in a relativistic plasma channel in the presence of a radial electron density gradient is experimentally shown for the first time. An inhomogeneous transverse density distribution was formed under the action of a powerful nanosecond pulse (10^{13} W cm^{-2}) on a thin mylar tape (15 μm). Heating and ablation lead to the tape boring with the formation of a plasma with a strong radial dependence of the concentration. The propagation of a relativistically intense femtosecond pulse (above

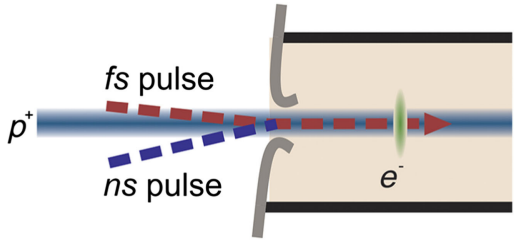

FIG. 9. Simplified model of the implementation of electron beam deflection approach to the AWAKE experiment.

10^{18} W cm^{-2}, 50 fs) through a plasma with a slight deviation relative to the breakdown symmetry axis is accompanied by refraction of the laser beam on the density gradient. It has been numerically established that, within the framework of the considered model of the breakdown and boring of a tape target by nanosecond radiation, the deviation of the propagation axis of a femtosecond pulse from the breakdown symmetry axis of up to 10 μm leads to deflection of the generated electron beam by up to 10°, while the beam parameters maintain almost unchanged. The calculations are confirmed by experimental data, where a similar deflection of the electron beam is observed on the detector. In the proposed approach, there is no angular dispersion in the energy of particles in the beam during deflection compared to the use of magnetic optics. This keeps charge of the beam in a collimated form.

The experimental approach can be used to create injector of preaccelerated particles into lateral energy gain stages, when each stage is pumped by a separate laser pulse [17,18]. From this point of view, the possibility of control of beam directionality is of high importance, since the electron bunch needs to be injected at a small angle to the axis of the next stage to avoid interference with optical and other mechanical components. For example, for the AWAKE experiment at CERN, the scheme could be drawn as in Fig. 9. Experimentally bunches from an rf accelerating structure with starting energy of ∼20 MeV were injected into the proton-driven wakefield and accelerated to 2 GeV [43]. However, injection of laser-generated electron bunch was also recently considered [19]. The femtosecond pulse in this case provides seed electrons for further acceleration in the wake of the proton driver. It was demonstrated that a few MeV electron beam with initial spectrum and divergence very similar to that we observe in our experimental scheme may be efficiently boosted up to 5 GeV after 10 m of acceleration. The tape target may serve as the entrance window of the gas cell, electron beam deflection eliminates optics on the proton beam path. At the same time, the proton beam deflection in the plasma channel may be neglected due to its large mass. In addition, the proposed method of electron beam deflection can serve not only for the tasks described above but also for diagnosing the interaction region: an optically opaque volume of dense plasma near the tape, the channel formed by a nanosecond pulse, and the radial density distribution in it can be indirectly estimated from angle of refraction of the escaping laser and particles beams.

ACKNOWLEDGMENTS

The work was carried out with the support of the Russian Science Foundation (Project No. 21-79-10207). A part of equipment was purchased with the support of the Ministry of Education and Science of the Russian Federation within the framework of the national project "Science and universities." The applicability of our approach for multistage electrons acceleration and AWAKE experiment was considered in the frame of scientific program of the National Center of Physics and Mathematics (project "Physics of high energy density. Stage 2023–2025").

[1] V. Malka, Phys. Plasmas **19**, 055501 (2012).
[2] C. Joshi, Plasma Phys. Controlled Fusion **61**, 104001 (2019).
[3] K. W. D. Ledingham and W. Galster, New J. Phys. **12**, 045005 (2010).
[4] T. Kurz *et al.*, Nat. Commun. **12**, 2895 (2021).
[5] T. Tajima and J. M. Dawson, Phys. Rev. Lett. **43**, 267 (1979).
[6] A. E. Hussein, A. V. Arefiev, T. Batson, H. Chen, R. S. Craxton, A. S. Davies, D. H. Froula, Z. Gong, D. Haberberger, Y. Ma, P. M. Nilson, W. Theobald, T. Wang, K. Weichman, G. J. Williams, and L. Willingale, New J. Phys. **23**, 023031 (2021).
[7] A. V. Arefiev, V. N. Khudik, A. P. L. Robinson, G. Shvets, L. Willingale, and M. Schollmeier, Phys. Plasmas **23**, 056704 (2016).
[8] H. Takabe and Y. Kuramitsu, High Power Laser Sci. Eng. **9**, e49 (2021).
[9] V. G. Nedorezov, S. G. Rykovanov, and A. B. Savel'ev, Phys. Usp. **64**, 1214 (2021).
[10] K. Nakajima, Proc. Jpn. Acad., Ser. B **91**, 223 (2015).
[11] L. Labate, D. Palla, D. Panetta, F. Avella, F. Baffigi, F. Brandi, F. Di Martino, L. Fulgentini, A. Giulietti, P. Köster, D. Terzani, P. Tomassini, C. Traino, and L. A. Gizzi, Sci. Rep. **10**, 17307 (2020).
[12] R. Antipenkov *et al.* in *High Power Lasers and Applications*, edited by J. Hein, T. J. Butcher, P. Bakule, C. L. Haefner, G. Korn, and L. O. Silva, *High Power Lasers and Applications* (SPIE, 2021), Vol. 11777, p. 117770E, 10.1117/12.2592432.
[13] H. T. Kim, K. H. Pae, H. J. Cha, I. J. Kim, T. J. Yu, J. H. Sung, S. K. Lee, T. M. Jeong, and J. Lee, Phys. Rev. Lett. **111**, 165002 (2013).
[14] X.-Z. Zhu, M. Chen, B.-Y. Li, F. Liu, X.-L. Ge, Z.-M. Sheng, and J. Zhang, Phys. Plasmas **29**, 013101 (2022).
[15] Z. Jin, H. Nakamura, N. Pathak, Y. Sakai, A. Zhidkov, K. Sueda, R. Kodama, and T. Hosokai, Sci. Rep. **9**, 20045 (2019).
[16] F. Massimo, A. Beck, J. Derouillat, M. Grech, M. Lobet, F. Pérez, I. Zemzemi, and A. Specka, Plasma Phys. Controlled Fusion **61**, 124001 (2019).

[17] E. M. Starodubtseva, I. N. Tsymbalov, K. A. Ivanov, D. A. Gorlova, and A. B. Savel'ev, Bulletin of the Lebedev Physics Institute **50**, S735 (2023).
[18] S. Steinke, J. van Tilborg, C. Benedetti, C. G. R. Geddes, C. B. Schroeder, J. Daniels, K. K. Swanson, A. J. Gonsalves, K. Nakamura, N. H. Matlis, B. H. Shaw, E. Esarey, and W. P. Leemans, Nature (London) **530**, 190 (2016).
[19] V. Khudiakov and A. Pukhov, Phys. Rev. E **105**, 035201 (2022).
[20] N. Moschuering, K. V. Lotov, K. Bamberg, F. Deutschmann, and H. Ruhl, Plasma Phys. Controlled Fusion **61**, 104004 (2019).
[21] V. Favaudon, L. Caplier, V. Monceau, F. Pouzoulet, M. Sayarath, C. Fouillade, M.-F. Poupon, I. Brito, P. Hupé, J. Bourhis, J. Hall, J.-J. Fontaine, and M.-C. Vozenin, Sci. Transl. Med. **6**, 245ra93 (2014).
[22] C. Gahn, G. D. Tsakiris, A. Pukhov, J. Meyer-ter Vehn, G. Pretzler, P. Thirolf, D. Habs, and K. J. Witte, Phys. Rev. Lett. **83**, 4772 (1999).
[23] K. Nakajima, Light Sci. Appl. **7**, 21 (2018).
[24] J. Luo, M. Chen, W. Y. Wu, S. M. Weng, Z. M. Sheng, C. B. Schroeder, D. A. Jaroszynski, E. Esarey, W. P. Leemans, W. B. Mori, and J. Zhang, Phys. Rev. Lett. **120**, 154801 (2018).
[25] D. E. Mittelberger, M. Thévenet, K. Nakamura, A. J. Gonsalves, C. Benedetti, J. Daniels, S. Steinke, R. Lehe, J.-L. Vay, C. B. Schroeder, E. Esarey, and W. P. Leemans, Phys. Rev. E **100**, 063208 (2019).
[26] C. qing Zhu, J. guang Wang, Y. fei Li, J. Feng, D. zhang Li, Y. hang He, J. hao Tan, J. long Ma, X. Lu, Y. tong Li, and L. ming Chen, Opt. Express **28**, 11609 (2020).
[27] I. Tsymbalov, D. Gorlova, K. Ivanov, S. Shulyapov, V. Prokudin, A. Zavorotny, R. Volkov, V. Bychenkov, V. Nedorezov, and A. Savel'ev, Plasma Phys. Controlled Fusion **63**, 022001 (2020).
[28] D. Gorlova, A. Y. Zavorotny, I. Tsymbalov, K. Ivanov, S. Shulyapov, R. Volkov, and A. Savel'ev, J. Surf. Invest.: X-Ray, Synchrotron Neutron Tech. **17**, 865 (2023).
[29] A. Y. Krukovskiy, V. G. Novikov, and I. P. Tsygvintsev, Math. Models Comput. Simul. **9**, 48 (2017).
[30] I. Vichev, A. Solomyannaya, A. Grushin, and D. Kim, High Energy Density Phys. **33**, 100713 (2019).
[31] S. Faik, A. Tauschwitz, and I. Iosilevskiy, Comput. Phys. Commun. **227**, 117 (2018).
[32] J. Derouillat, A. Beck, F. Pérez, T. Vinci, M. Chiaramello, A. Grassi, M. Flé, G. Bouchard, I. Plotnikov, N. Aunai, J. Dargent, C. Riconda, and M. Grech, Comput. Phys. Commun. **222**, 351 (2018).
[33] A. Pukhov and J. Meyer-ter Vehn, Phys. Plasmas **5**, 1880 (1998).
[34] S. J. E. Brockington, R. D. Horton, D. Q. Hwang, R. W. Evans, S. J. Howard, and Y. C. F. Thio, Rev. Sci. Instrum. **76**, 063503 (2005).
[35] C. L. Enloe, R. M. Gilgenbach, and J. S. Meachum, Rev. Sci. Instrum. **58**, 1597 (1987).
[36] A. Pukhov and J. Meyer-ter Vehn, Phys. Rev. Lett. **76**, 3975 (1996).
[37] A. Sharma, D. V. Kumar, and A. K. Ghatak, Appl. Opt. **21**, 984 (1982).
[38] R. Babjak, L. Willingale, A. Arefiev, and M. Vranic, Phys. Rev. Lett. **132**, 125001 (2024).
[39] S. Rae, Opt. Commun. **97**, 25 (1993).
[40] L. Labate, M. G. Andreassi, F. Baffigi, R. Bizzarri, A. Borghini, G. C. Bussolino, L. Fulgentini, F. Ghetti, A. Giulietti, P. Köster, D. Lamia, T. Levato, Y. Oishi, S. Pulignani, G. Russo, A. Sgarbossa, and L. A. Gizzi, J. Phys. D Appl. Phys. **49**, 275401 (2016).
[41] C. E. Doss, R. Ariniello, J. R. Cary, S. Corde, H. Ekerfelt, E. Gerstmayr, S. J. Gessner, M. Gilljohann, C. Hansel, B. Hidding, M. J. Hogan, A. Knetsch, V. Lee, K. Marsh, B. O'Shea, P. San Miguel Claveria, D. Storey, A. Sutherland, C. Zhang, and M. D. Litos, Phys. Rev. Accel. Beams **26**, 031302 (2023).
[42] X. Zhu, B. Li, F. Liu, J. Li, Z. Bi, X. Ge, H. Deng, Z. Zhang, P. Cui, L. Lu, W. Yan, X. Yuan, L. Chen, Q. Cao, Z. Liu, Z. Sheng, M. Chen, and J. Zhang, Phys. Rev. Lett. **130**, 215001 (2023).
[43] E. Adli *et al.*, Nature (London) **561**, 363 (2018).